

Two-dimensional topological semimetals protected by symmorphic symmetries

Wei Luo,^{1,2,*} Junyi Ji,^{1,2,*} Jinlian Lu,^{1,2} Xiuwen Zhang,^{3,†} and Hongjun Xiang^{1,2,‡}

¹*Department of Physics, Key Laboratory of Computational Physical Sciences (Ministry of Education), State Key Laboratory of Surface Physics, Fudan University, Shanghai 200433, People's Republic of China*

²*Collaborative Innovation Center of Advanced Microstructures, Nanjing 210093, People's Republic of China*

³*College of Electronic Science and Technology, Shenzhen University, Shenzhen 518060, People's Republic of China*



(Received 30 October 2019; revised manuscript received 17 April 2020; accepted 17 April 2020; published 5 May 2020)

Two-dimensional (2D) band crossing semimetals (BCSMs) could be used to build a range of novel nanoscale devices, such as superlenses and transistors. We find that symmorphic symmetry can protect a new type of robust 2D BCSM, unlike the previously proposed 2D essential BCSMs protected by nonsymmorphic symmetry [Young and Kane, *Phys. Rev. Lett.* **115**, 126803 (2015)]. This type of symmorphic symmetry-protected (SSP) 2D essential BCSM cannot be pair annihilated without destroying the crystalline symmetries as opposed to the 2D BCSM caused by the accidental band crossing. Through group-theory analysis, we find that 2D SSP BCSMs can only exist at the $K(K')$ point of the Brillouin zone of four-layer groups and identify nonmagnetic 2D FeB_2 as a candidate. Interestingly, nonmagnetic 2D SSP BCSMs can host a single pair of band crossing points (BCPs), whereas nonmagnetic three-dimensional Weyl semimetals have, at least, two pairs of band crossing Weyl points. It is found that the single pair of BCPs is robust against any kind of strain. Furthermore, our calculation suggests that essential 2D SSP BCSMs can be used to realize electric-field control of spin texture and, thus, are promising candidates for spintronic devices.

DOI: [10.1103/PhysRevB.101.195111](https://doi.org/10.1103/PhysRevB.101.195111)

I. INTRODUCTION

Three-dimensional (3D) Weyl semimetals (WSMs) [1,2] in which two bands cross with each other linearly in momentum space near the Fermi level have attracted great interest due to their novel transport properties, such as the chiral anomaly effect [3–5], the anomalous Hall effect [6–10], and the intrinsic spin Hall effect [11]. More interestingly, 3D WSMs host the topologically protected Fermi arc [1,6,12], which are distinguished from the topological surface states of topological insulators and Chern insulators. Weyl points (WPs) in 3D WSMs must exist in pairs due to the conservation of chirality [13–15] which is forced by the no-go theorem [16], hence, are robust to perturbation without breaking the translational symmetry [17]. The only way to annihilate them is letting them meet with each other at a point in the Brillouin zone (BZ), consequently, forming a Dirac point or opening a band gap.

Although 3D WSMs were widely studied in recent years [2,8,17–24], there are only a few studies on their analogies [25–29], i.e., “two-dimensional (2D) band crossing semimetals (BCSMs).” Similar with the 3D WPs, the 2D band crossing WPs also maintain linear dispersions near band crossing points (BCPs). The 2D BCSMs could display extraordinary properties, for instance, the nonlinear anomalous Hall effect in 2D WTe_2 [30]. Generally speaking, considering whether

BCPs can be pairwise annihilated or not without breaking the system's crystalline symmetries, 2D BCSMs can be classified into two categories. For the first category, the BCPs are caused by accidental band crossing and can be pairwise annihilated while preserving the crystalline symmetries. Park and Yang systematically investigated these kinds of 2D BCSMs [31]. The potassium-doped few-layer black phosphorus [32], $1T'$ monolayer of WTe_2 with an electric field perpendicular to the 2D plane [30] and 2D TiB_2 [33] belong to this category. For the second category, the BCPs cannot be pairwise annihilated as long as the crystalline symmetries are preserved—we, thus, refer to them as 2D essential BCSMs. These kinds of BCSMs have been theoretically discussed in nonsymmorphic layer groups (LGs) [34]. However, no material candidates have been proposed for the nonsymmorphic symmetry-protected 2D essential BCSMs. For symmorphic LGs, it was widely believed that the 2D essential BCSMs can only be enforced by the Kramers theorem [34,35].

In this article, we propose that 2D essential BCSMs can emerge in symmorphic LGs, which arise from the spatial symmetries instead of the Kramers degeneracy. Based on systematic group-theory analysis, we find that SSP 2D essential BCSMs can only exist at the $K(K')$ point of the BZ of four LGs (67, 70, 76, and 77). Interestingly, 2D SSP essential BCSMs can host a single pair of BCPs when preserve the time-reversal (TR) symmetry and break the inversion symmetry, different from the 3D time-reversal invariant (TRI) WSMs that host, at least, two pairs of WPs [36]. This character makes the SSP 2D essential BCSMs an ideal platform for detecting the BCPs. We note that the 2D FeB_2 material [37] (layer group index 77) hosts only one pair of ideal BCPs at the Fermi

*These authors contributed equally to this work.

†xiuwenzhang@szu.edu.cn

‡hxiang@fudan.edu.cn

level which is protected by the pure symmorphic symmetries without involving the TR symmetry. Interestingly, we find that the BCPs in FeB₂ are robust for large uniaxial strain ($\sim 25\%$) which is similar with the robustness of Dirac points in graphene under strain [38,39].

II. DESIGN PRINCIPLES FOR THE SSP 2D ESSENTIAL BCSM FROM GROUP-THEORY ANALYSIS

BCSMs are formed due to the doubly degenerate band crossing points in the BZ of materials with either broken TR or spatial inversion symmetry (similar to that of 3D WSMs). For symmorphic LGs, there are no nonsymmorphic symmetries to stick a certain minimal number of bands together [34,40]. In this case, it is believed [34] that only TR symmetry can group two bands together (filling of an odd number of electrons will lead to WPs at TRI points). However, if we inspect the character table of irreducible representations (IRs) for symmorphic LGs, we find that there exist some two-dimensional IRs. This means that 2D essential BCPs may be maintained solely by symmorphic symmetries. Note that two-dimensional IRs for symmorphic LGs are only available at high-symmetry points and lines. However, the 2D essential BCPs can only exist at high-symmetry points, instead, of lines since the twofold essential degeneracy must split along different directions near the BCPs. For 2D systems, the high-symmetry points in the BZ include only six points. They are $\Gamma(0,0)$, $X(0.5,0)$, $Y(0,0.5)$, $M(0.5,0.5)$, $K(1/3,1/3)$, and $K'(-1/3,-1/3)$. Since we are focusing on the SSP 2D essential BCSMs, the BCPs located at the TR invariant points (Γ , X , Y , and M) that are protected by the TR symmetry [35] are excluded. Hence, the SSP essential BCPs must locate at $K(1/3,1/3)$ or $K'(-1/3,-1/3)$. Namely, the SSP 2D essential BCSMs can only exist in the hexagonal/trigonal systems. For the SSP 2D essential BCSMs, there are two different cases. For the first case, a band is singly degenerate near $K(K')$ in the BZ without considering the spin-orbit coupling (SOC) effect. After considering the SOC effect, in order to realize the BCSMs phase, the IR of this band should belong to a two-dimensional IR at the $K(K')$ point and decompose to two one-dimensional IRs near $K(K')$ (see Appendix A). Note that the BCPs, in this case, have the same electron filling condition with that of TR-protected BCPs (i.e., filling of odd number of electrons). Hence, we will not discuss this case hereafter (details about these kinds of BCPs can be seen from Appendix A). For the second case, without considering the SOC effect, the band belongs to a two-dimensional IR at $K(K')$. After considering the SOC effect, the two-dimensional IR will decompose to two two-dimensional [2 + 2 mode, Fig. 1(a)] or one two-dimensional and two one-dimensional [2 + 1 + 1 mode, Fig. 1(b)] IRs according to their symmetry at the $K(K')$ point. For the 2 + 2 mode, it will cause a band gap at the K point, so we exclude this case. For the 2 + 1 + 1 mode (the band decomposition can be deduced based on the group theory, see Appendix A) due to the different SOC form, the energy levels for the one doubly degenerated as well as the two singly degenerated bands can be different. Here, we are only interested in the case where the BCPs locate at the Fermi level as illustrated in Fig. 1(b).

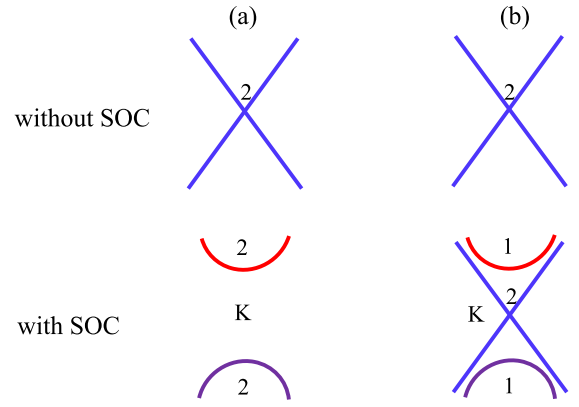


FIG. 1. Schematic for searching the 2D SSP BCSMs. (a) Without the SOC effect, the band is doubly degenerated at the K point. After considering the SOC effect, the doubly degenerated bands split into two twofold degeneracy bands and form a band gap at the K point. (b) After considering the SOC effect, the doubly degenerated bands split into one twofold degeneracy band and two onefold degeneracy bands. Thus, form the BCPs at the K point.

It is noted that our discussion on SSP 2D essential BCSMs is limited to TRI systems. Based on the above analysis, for realizing the SSP 2D essential BCSMs, the system should satisfy four conditions: (I) the breaking of inversion symmetry since the system adopts TR symmetry; (II) the lattice maintains the hexagonal or trigonal symmetry; (III) the little group of the $K(K')$ point should have a two-dimensional IR without considering the SOC effect, which decomposes to one two-dimensional and two one-dimensional IRs after considering SOC; (IV) the band dispersion near the crossing point (i.e., K or K') should be linear. The symmorphic LGs can be obtained by removing the T and O point groups from the 3D point groups. From the table of 80 LGs [41], one can easily obtain the 36 symmorphic LGs. Considering the first condition, i.e., removing the groups with inversion symmetry, there remain 25 LGs. Then, the second condition requires that the lattice maintains the hexagonal/trigonal symmetry (with the C_3 or C_6 rotation axis). Thus, there remain 11 LGs. Considering the third condition, the number of candidate LGs shrinks to 4. Their indices are 67, 70, 76, and 77, corresponding to D_3-2 , $C_{3v}-2$, D_6 , and C_{6v} point groups. For the last condition, if the symmetric Kronecker product $[R_k \times R_k]$ [R_k represents the two-dimensional IR at $K(K')$ in the BZ] of the two-dimensional IR with itself contains the vector representation of G_k [G_k is the little group at the $K(K')$ point], the linear dispersion can be guaranteed [42]. We find that this condition does not exclude any of the remaining four LGs (67, 70, 76, and 77). Based on the above analysis, the searching of SSP 2D essential BCSMs can be conducted as follows [see Fig. 1(b)]: first, finding the band crossing belonging to a two-dimensional IR at K without considering the SOC effect. Then, finding the cases in which after including the SOC effect, the two-dimensional IR splits into a two-dimensional IR with linear dispersion and two one-dimensional IRs as illustrated in Fig. 1(b).

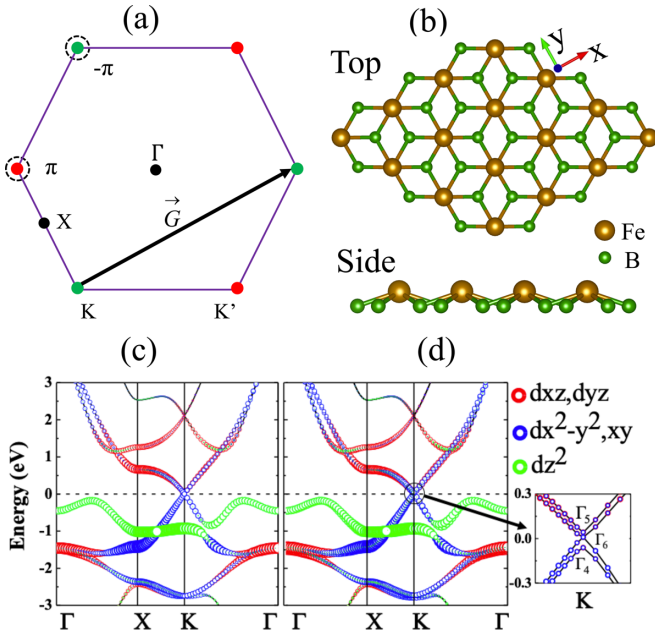


FIG. 2. (a) The BZ for 67, 70, 76, and 77 LGs. The two BCPs are located at the K point and its time-reversal partner K' . (b) Top and side views of the 2D FeB_2 system. (c) Band structure for the 2D FeB_2 system without considering the SOC effect. The crossing bands are contributed by the (d_{xz}, d_{yz}) and $(d_{x^2-y^2}, d_{xy})$ orbitals. (d) Band structure with the SOC effect taken into account. The bands split into two onefold degenerated bands and one twofold degenerated band, forming the ideal band crossing semimetal.

III. TWO-DIMENSIONAL ESSENTIAL BCPS IN THE FeB_2 SYSTEM

We find that the FeB_2 monolayer [37] [see Fig. 2(b)] with a graphenelike boron sheet is a candidate SSP 2D essential BC-SMs which belongs to the No. 77 (C_{6v}) layer group. The band structures of FeB_2 calculated by using first-principles calculations (see Appendix B) without/with the SOC effect are shown in Figs. 2(c) and 2(d), respectively. From Fig. 2(c), we can see that the wave function belongs to the two-dimensional IR Γ_3 of the single group of C_{3v} at the $K(1/3, 1/3)$ point, and that the band crossing is mainly contributed by the Fe $(d_{x^2-y^2}, d_{xy})$ and (d_{xz}, d_{yz}) orbitals. Here, it is noted that the $(d_{x^2-y^2}, d_{xy})$ and (d_{xz}, d_{yz}) orbitals maintain the same transformation character under the C_{3v} point group. In other words, they belong to the same two-dimensional IR Γ_3 of C_{3v} . After considering the SOC effect, the direct product of Γ_3 and spin representation $D_{1/2}$ is decomposed into one Γ_4 (one-dimensional), one Γ_5 (one-dimensional), and one Γ_6 (two-dimensional) IRs [see Fig. 2(d)]. Since the energy order is computed to be $\Gamma_4 < \Gamma_6 < \Gamma_5$, the Weyl point locates exactly at the Fermi level as shown in Fig. 2(d), forming a SSP 2D ideal essential BC-SM.

IV. LOW-ENERGY EFFECTIVE HAMILTONIAN OF FeB_2

At the K point, the little point group is C_{3v} , and the crossing bands belong to the Γ_3 (two-dimensional) IR without considering the SOC effect. Based on the theory of invariants [43], we derive the low-energy effective Hamiltonian of the 2D FeB_2 system with/without the SOC effect. Without the

SOC effect, the bases which transform according to the Γ_3 IR can be written as $|\phi_1\rangle$ and $|\phi_2\rangle$. The low-energy effective Hamiltonian at the K point is written as

$$H_K = \begin{pmatrix} C_0 & C_2 k_+ \\ C_2 k_- & C_0 \end{pmatrix},$$

where $k = k' - K$ and k' is a point near the K point ($k_{\pm} = k_x \pm ik_y$). C_0 and C_2 are constants. It is clear that the two bands with the eigenvalues $E_{1,2}(k) = C_0 \pm C_2 \sqrt{k_x^2 + k_y^2}$ degenerate with each other at the K point. From the eigenvalues, one can see that the two bands maintain isotropic linearly dispersion near the K point. After considering the SOC effect since the spin degree is included, the bases change to be $|\phi_{1\uparrow}\rangle$, $|\phi_{1\downarrow}\rangle$, $|\phi_{2\uparrow}\rangle$, and $|\phi_{2\downarrow}\rangle$. The low-energy effective Hamiltonian (details can be seen in Appendix C) at the $K(1/3, 1/3)$ point becomes a 4×4 matrix,

$$H = \begin{pmatrix} c_0 & -\frac{a_1+b_1}{\sqrt{2}}k_- & -i\frac{a_1-b_1}{\sqrt{2}}k_- & ic_1k_+ \\ -\frac{a_1+b_1}{\sqrt{2}}k_+ & \frac{a_0+b_0}{2} & i\frac{a_0-b_0}{2} & i\frac{a_1-b_1}{\sqrt{2}}k_- \\ i\frac{a_1-b_1}{\sqrt{2}}k_+ & -i\frac{a_0-b_0}{2} & \frac{a_0+b_0}{2} & \frac{a_1+b_1}{\sqrt{2}}k_- \\ -ic_1k_- & -i\frac{a_1-b_1}{\sqrt{2}}k_+ & \frac{a_1+b_1}{\sqrt{2}}k_+ & c_0 \end{pmatrix},$$

where a_0 , a_1 , b_0 , b_1 , c_0 , and c_1 are real constants and $i = \sqrt{-1}$. One can see that the eigenvalues are $E_{1,2} = c_0$, $E_3 = a_0$, and $E_4 = b_0$ at the $K(1/3, 1/3)$ point. $E_{1,2}$ is twofold degenerated, whereas E_3 and E_4 are not degenerated with each other at $K(1/3, 1/3)$, and there exists a $|b_0 - a_0|$ energy gap between them. Away from the K point, the dispersion of the two bands close to the Fermi level is linear (see Appendices A and C). From the effective Hamiltonian analysis, we can easily see that due to the SOC effect, the spinless BCPs (not including spin) change into the spinful BCPs (including spin), which agrees with the motif described by Fig. 1(b).

V. THE EMERGENCE OF A SINGLE PAIR OF BCPS IN 2D NONMAGNETIC SYSTEMS

For these four-layer groups, the shapes of their BZs are the same as shown in Fig. 2(a). Since K and K' are related by the TR symmetry, the BCPs must locate at K and K' simultaneously, leading to a single pair of BCPs that is very different from the 3D WPs. For 3D nonmagnetic WSMs, there exist, at least, two pairs of WPs in the BZ [36] because a Weyl point located at a k point in the BZ is converted into another Weyl point at the $-k$ point with the same chirality due to the TR symmetry. Based on the no-go theorem [13], there must exist another pair of WPs with the opposite chirality. However, for 2D BCPs, the concept of the chirality of a “magnetic monopole” is not well defined. Hence, a single pair of BCPs in a 2D nonmagnetic system is allowed. This new feature of 2D BC-SMs provides a good platform for the experimental study of the 2D BCPs. It is noted that the number of 2D BCPs must be even since the sum of Berry phases around BCPs must equal to zero (or integral multiple of 2π) [25] in the whole 2D BZ. In addition, by combining the maximally localized Wannier functions [44,45] and WANNIERTOOLS [46], we find that there are nontrivial edge states for zigzag FeB_2 nanoribbons (see Appendix D).

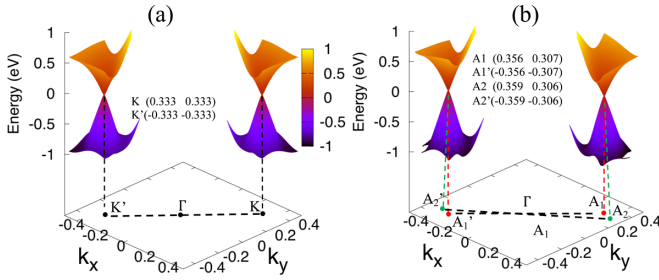


FIG. 3. The band structure for the FeB_2 system near the K and K' points with the SOC effects. (a) Without strain and (b) with 5% uniaxial [along the x (zigzag) direction, see Fig. 2(b)] tensile strain. After adding the tensile strain, the BCPs shift their positions and evolve into two pair of BCPs.

VI. STRAIN-ROBUST 2D BCPs IN A FeB_2 SYSTEM

We checked the stability of BCPs under different kinds of strain and find that they are robust against any kind of strain (uniaxial and shear strain). Especially, BCPs in 2D FeB_2 cannot be annihilated even under 25% uniaxial tensile (reducing C_{6v} to C_2) strain. For comparison, we plot band structures near the BCPs without/with 5% tensile strain with considering SOC effects (Fig. 3). One can easily find that BCPs have shifted away from the high-symmetry K point under strain. Another interesting result is that one pair of BCPs (without strain) evolve into two pair of BCPs under strain. As shown in Fig. 3(b), two BCPs are very close to each other under strain. Note that there is only one pair of BCPs under strain if we do not consider the SOC effect. The formation of two pair of BCPs with considering SOC effects is forced by the rotation anomaly [47]. The robustness of the BCPs in the FeB_2 system under strain without considering SOC effects is similar with that of the robust Dirac points in graphene [38] which is protected by the space-time inversion symmetry [48–50]. Here, we find that BCPs in FeB_2 are protected by the combined operation of C_{2z} rotation and TR symmetry. We check the different kinds of strain and find that they do not destroy the C_{2z} rotation symmetry, thus, the $C_{2z}T$ combined symmetry is still maintained, leading to the robustness of BCPs under different kinds of strain. Since the 67 ($D_{3d}-2$) and 70 ($C_{3v}-2$) LGs does not include a C_{2z} rotation axis, the BCPs in these two groups are not robust under uniaxial and shear strain, i.e., for SSP 2D essential BCSMs, only the 76 and 77 LGs can maintain the robust BCPs under various strains. It is noted that the strain here changes the category of BCPs (i.e., from the second category to the first category). After adding the uniaxial tensile strain, the BCPs are caused by accident band crossing and can be eliminated by merging two BCPs at the TR invariant points [39]. Note that here the accident band crossing is protected by the combined operation of C_{2z} and TR symmetry that is different than the BCPs located at the high-symmetry line or plane, which is caused by two different one-dimensional IRs (the crossing bands maintain different eigenvalues) and is locally protected by a single-crystal symmetry (such as rotation and mirror symmetry) without involving TR symmetry.

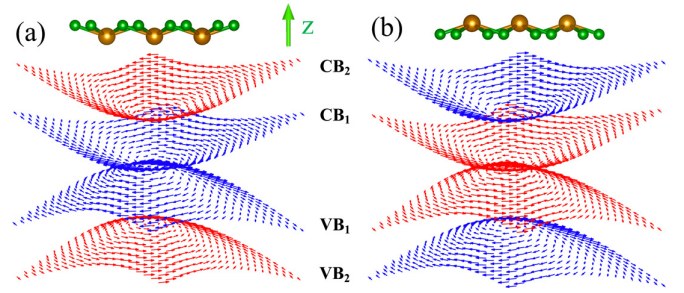


FIG. 4. The Rashba-like spin texture of the top two VBs and lowest two CBs for the FeB_2 system with polarization along the (a) $-z$ and (b) $+z$ directions. Note that the energy levels of VB_2 and CB_2 have been shifted 0.1 eV relative to that of VB_1 and CB_1 in order to make the spin texture clearer. The blue and red colors indicate clockwise and anticlockwise, respectively. One can easily find the helicity of the spin texture has been reversed due to the reverse of the polarization.

VII. SPIN-TEXTURE CONTROLLED BY THE ELECTRIC FIELD

Since the FeB_2 monolayer adopts a buckled crystal structure, it has an intrinsic nonzero electric polarization along the z direction. Hence, we speculate that it may maintain a Rashba-like spin texture. Using first-principles calculations, we calculate the spin texture for the 2D FeB_2 system (Fig. 4). One can see that the first valence-band maximum (VBM_1) [first conduction-band minimum (CBM_1)] and VBM_2 (CBM_2) adopt opposite spin-texture helicities. However, for VBM_1 and CBM_1 , they maintain the same spin-texture helicity. As K and K' also adopt the same spin-texture helicity due to the TR symmetry, the electronic states near the Fermi surface of the FeB_2 monolayer maintain a single spin-texture helicity. It is noted that, here, the spin expectation value for VBM_2 and CBM_2 should be zero at the K and K' points. This can be understood easily based on the group theory. The K and K' points have the C_{3v} little group. The invariant representation of C_{3v} does not include the pseudospin vector (in other words, C_{3v} is a non-pseudopolar point group [51]). Hence, the spin should be zero for singly degenerated band VBM_2 and CBM_2 . After reversing the electric polarization in the z direction, i.e., switching the position of Fe and B atoms, the spin textures are totally reversed, thus, realizing the electric-field control of Rashba-like spin texture. This can be understood as follows: The two states (polarization along z and $-z$, respectively) are related by an in-plane mirror symmetry operation, which does not change the k point but reverses the in-plane components of the spin vectors. This result can also be deduced from our previous low-energy effective Hamiltonian. We note that the band splitting away from the Weyl point is also fundamentally different from the usual Rashba splitting: (1) It does not take place at a TRI k point; (2) the spin textures of the two bands near the Fermi level have the same chirality.

It is noted that, although this system is metallic (strictly speaking, semimetallic), the electric polarization might be reversed since the electrons are not allowed to move along

the z direction [52,53], and the electronic screening effect for the electric field is weak due to the semimetallic nature of the electronic structure. Hence, our works suggest the reversal of the spin texture in 2D BCSMs by an external electric field, which may broaden the way for topological quantum spintronics.

VIII. CONCLUSIONS

To summarize, we demonstrated that 2D SSP essential BCSMs can only exist in 67, 70, 76, and 77 layer groups. Interesting, these kinds of 2D BCSMs can maintain a single pair of BCPs in the BZ. We find that the 2D buckled FeB_2 belonging to the layer group 77, is a candidate for 2D SSP essential BCSMs. Remarkably, the BCPs in this system are robust for different kinds of strain, and even the 25% uniaxial tensile strain cannot annihilate the BCPs. Moreover, our calculations indicate that the FeB_2 system adopts a Rashba-like spin texture near the $K(K')$ point and a single spin-texture helicity for all the electronic states near the Fermi surface. When the polarization is reversed, the Rashba-like spin-texture helicity is also reversed, realizing the electric-field control of Rashba-like spin texture in semimetallic systems. Since the BCPs exactly locate at the inequivalent K and K' valleys, these kinds of 2D essential BCSMs represent a good platform for studying topological valleytronics.

ACKNOWLEDGMENTS

Work at Fudan was supported by NSFC Grant No. 11825403, the Program for Professor of Special Appointment (Eastern Scholar), the Qing Nian Ba Jian Program, and the Fok Ying Tung Education Foundation. Work at Shenzhen was supported by NSFC Grants No. 11774239 and No. 61827815.

APPENDIX A: DETAILED GROUP-THEORY ANALYSIS ON THE CONDITION OF THE EXISTENCE OF BCPs

As shown in the main text, four-layer groups (Nos. 67, 70, 76, and 77) may host 2D Weyl points. Here, we now demonstrate in detail that this is, indeed, the case. For layer groups 67 and 76 (D_{3-2} and D_6), the little group of $K(K')$ points is D_3 . For layer groups 70 and 77 (C_{3v-2} and C_{6v}), the little group of $K(K')$ points is C_{3v} . Our analysis shows that the D_3 case is similar to the C_{3v} case. Here, we take the C_{3v} point group to illustrate the detailed analysis process. The character table of C_{3v} is shown in Table I. The letter O represents the

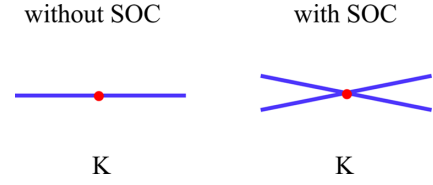


FIG. 5. Without the SOC effect, for the $K(K')$ point, the band is singly degenerate. After considering the SOC effect, the band is double degenerate at the K point and split away from the K point, leading to BCPs. These kinds of BCPs require the same filling condition (odd number of electrons) as that of time-reversal symmetry-protected BCPs.

different classes for the C_{3v} point group with considering the spin degree. Γ_1 , Γ_2 , and Γ_3 are the representation of a single group of the C_{3v} point group. Γ_4 , Γ_5 , and Γ_6 are additional representations which involve the SOC effect. $D_{1/2}$ represents the spin representation.

First, we discuss the first case (see Fig. 5) where the band at the K point is singly degenerate when the SOC effect is not included. After considering the SOC effect, it becomes double degenerate. To see how the bands split after considering the SOC effect, we should consider the decomposition of the direct-product representation between a one-dimensional representation (Γ_1 or Γ_2) and the spin representation $D_{1/2}$. Thus, we should get the character of the spin representation $D_{1/2}$ first. If an operation O is a proper rotation with the rotation angle α , the character of spin representation $D_{1/2}$ can be obtained from the formula,

$$\chi^j(\alpha) = \frac{\sin(j + \frac{1}{2})}{\sin(\frac{\alpha}{2})}.$$

Here, j is chosen to be $1/2$. For improper rotation, one can decompose it to the product between a proper rotation and the inversion I . Since the $D_{1/2}$ spin representation is invariant under the inversion I [54], we also can obtain the character of spin representation $D_{1/2}$ by using the above formula. The obtained characters of spin representation $D_{1/2}$ are shown in Table I. One can easily get $\Gamma_1 \otimes D_{1/2} = \Gamma_6$ and $\Gamma_2 \otimes D_{1/2} = \Gamma_6$. This result indicates that after considering the SOC effect, the singly degenerated band will become double degenerate bands at the K point. Near the $K(K')$ point, the dispersion is linear. This can be explained from group theory. First, after considering the SOC effect, the bands belong to the Γ_6 representation at the K point. Since the Kronecker product

TABLE I. The character table for the C_{3v} double point group.

	O_1	O_2	O_3	O_4	O_5	O_6	
Γ_1	1	1	1	1	1	1	$O_1: E$
Γ_2	1	1	-1	1	1	-1	$O_2: C_{3(001)}^1, \bar{C}_{3(001)}^2$
Γ_3	2	-1	0	2	-1	0	$O_3: m_{1-10}, m_{120}, m_{210}$
Γ_4	1	-1	$-i$	-1	1	i	$O_4: \bar{E}$
Γ_5	1	-1	i	-1	1	$-i$	$O_5: C_{3(001)}^2, \bar{C}_{3(001)}^1$
Γ_6	2	1	0	-2	-1	0	
$D_{1/2}$	2	1	0	-2	-1	0	$O_6: \bar{m}_{1-10}, \bar{m}_{120}, \bar{m}_{210}$

$\Gamma_6 \otimes \Gamma_6$ can be decomposed into $\Gamma_1 + \Gamma_2 + \Gamma_3$ and the IR Γ_3 is a vector representation of the little group C_{3v} , indicating that the linear dispersion must be guaranteed. Thus, there is a band crossing point at the $K(K')$ point after the SOC effect is included for a singly degenerate band before the SOC effect is included.

Now, we turn to the second case where the bands at the K point belong to a two-dimensional representation. The single point-group representation of C_{3v} only has one twofold IR Γ_3 . The direct product representation between Γ_3 and $D_{1/2}$ is $\Gamma_3 \otimes D_{1/2} = \Gamma_4 + \Gamma_5 + \Gamma_6$. This indicates that the band will split into a double degenerate band and two single degenerate bands after considering the SOC effect. Near the $K(K')$ point, the dispersion is linear, which can be proved as follows. Considering the SOC effect, we have $\Gamma_3 \otimes D_{1/2} = \Gamma_4 + \Gamma_5 + \Gamma_6$. The two crossing bands belongs to the twofold IR Γ_6 . Since the Kronecker product $\Gamma_6 \otimes \Gamma_6$ can be decomposed into $\Gamma_1 + \Gamma_2 + \Gamma_3$, and the Γ_3 IR is a vector representation of the little group C_{3v} , indicating that the linear dispersion must be guaranteed. Thus, there is a band crossing point at the $K(K')$ point after the SOC effect is included for double degenerate bands before the SOC effect is included.

APPENDIX B: DETAILS OF FIRST-PRINCIPLES CALCULATIONS

In this paper, the density functional theory (DFT) method is used for structural relaxation and electronic structure calculation. The ion-electron interaction is treated by the projector augmented-wave [55] technique as implemented in the Vienna *ab initio* simulation package [56]. The exchange-correlation potential is treated by the generalized gradient approximation in the Perdew-Burke-Ernzerhof form [57]. For structural relaxation, all the atoms are allowed to relax until atomic forces are smaller than 0.01 eV/Å. The 2D k mesh is generated by the Monkhorst-Pack scheme. To avoid the interaction between neighboring layers, the vacuum thickness is chosen to be 13 Å.

APPENDIX C: MODEL HAMILTONIAN DERIVED WITH THE INVARIANT METHOD

In this part, we derive the effective model Hamiltonian with the invariant method. According to group theory, applying an operator $\hat{g} \in G$ (G is the symmetry group of the system) to the basis functions $\{\varphi_i\}$, the new functions can be expressed as a linear combination of the basis functions,

$$\hat{g}\varphi_i = \sum_j D_{ji}(\hat{g})\varphi_j.$$

These matrices $D(\hat{g})$ form a representation of G .

Based on the theory of invariants [58], the Hamiltonian must satisfy the condition,

$$D^{-1}(\hat{g})H(\kappa)D(\hat{g}) = H(\hat{g}^{-1}\kappa), \quad \hat{g} \in G.$$

In general, $D(\hat{g})$ is reducible and can be decomposed into different IRs,

$$D(\hat{g}) = \sum_{i=1}^n \oplus \Gamma^i(\hat{g}).$$

Then, the Hamiltonian can be decomposed into the submatrix according to the IRs,

$$\hat{H}(\kappa) = \begin{pmatrix} \hat{H}^{11} & \cdots & \hat{H}^{1n} \\ \vdots & \ddots & \vdots \\ \hat{H}^{n1} & \cdots & \hat{H}^{nn} \end{pmatrix}.$$

Since $D(\hat{g})$ is block diagonal, the invariance of the Hamiltonian yields the following relations for each submatrix:

$$\hat{\Gamma}^\alpha(\hat{g}^{-1})\hat{H}^{\alpha\beta}(\kappa)\hat{\Gamma}^\beta(\hat{g}) = \hat{H}^{\alpha\beta}(\hat{g}^{-1}\kappa),$$

where $\hat{H}^{\alpha\beta}(\kappa)$ is a $d_\alpha \times d_\beta$ matrix and d_α is the dimension of IR α .

The submatrices $\hat{H}^{\alpha\beta}(\kappa)$ can be formed by the products between representation matrices $\hat{X}_l^\gamma(\tau|\alpha, \beta)$ and the corresponding basis functions $H_l^\gamma(\kappa)$, which transform according to complex conjugate IR $\bar{\gamma}$,

$$\begin{aligned} \hat{H}^{\alpha\beta}(\kappa) &= \sum_\tau \sum_{\gamma, l} \hat{X}_l^\gamma(\tau|\alpha, \beta) H_l^{\bar{\gamma}}(\kappa), \\ \hat{\Gamma}^{\bar{\alpha}} \otimes \hat{\Gamma}^\beta &= \sum_\gamma \oplus a_\gamma \hat{\Gamma}^\gamma, \\ a_\gamma &= \frac{1}{|G|} \sum_{g \in G} \bar{\chi}^\gamma \bar{\chi}^\gamma(g) \bar{\chi}^\alpha(g) \chi^\beta(g), \\ \tau &= 1, 2, \dots, a_\gamma. \end{aligned}$$

$X_l^\gamma(\tau|\alpha, \beta)$ can be figured out by

$$[X_l^\gamma(\tau|\alpha, \beta)]_{i,j} \sim \begin{pmatrix} \alpha & \tau \\ i & l \end{pmatrix} \begin{pmatrix} \bar{\gamma} & \beta \\ l & j \end{pmatrix},$$

where $\begin{pmatrix} \alpha & \tau \\ i & l \end{pmatrix} \begin{pmatrix} \bar{\gamma} & \beta \\ l & j \end{pmatrix}$ is the Clebsch-Gordan coefficient.

At the K point, the little point group is C_{3v} , and the crossing bands belong to the two-dimensional IR Γ_3 without considering the SOC effect. We can define two bases as $|\phi_1\rangle$ and $|\phi_2\rangle$, which transform as the two-dimensional IR Γ_3 . Based on these two bases, the representation matrix of space-group operators at the K point can be written as

$$\begin{aligned} D(g_1) &= \begin{pmatrix} 1 & 0 \\ 0 & 1 \end{pmatrix}, \quad D(g_2) = \begin{pmatrix} e^{i\theta} & 0 \\ 0 & e^{-i\theta} \end{pmatrix}, \\ D(g_3) &= \begin{pmatrix} e^{-i\theta} & 0 \\ 0 & e^{i\theta} \end{pmatrix}, \\ D(g_4) &= \begin{pmatrix} 0 & 1 \\ 1 & 0 \end{pmatrix}, \quad D(g_5) = \begin{pmatrix} 0 & e^{-i\theta} \\ e^{i\theta} & 0 \end{pmatrix}, \\ D(g_6) &= \begin{pmatrix} 0 & e^{i\theta} \\ e^{-i\theta} & 0 \end{pmatrix}, \quad \theta = \frac{2\pi}{3}. \end{aligned}$$

Here, we define $\mathbf{a} = (\frac{1}{2}, -\frac{\sqrt{3}}{2}, 0)$, $\mathbf{b} = (\frac{1}{2}, \frac{\sqrt{3}}{2}, 0)$, and $\mathbf{c} = (0, 0, 1)$. $g_1 = E$ is the invariant operator, $g_2 = 3_{001}^+$ is the anticlockwise threefold rotation around the c axis, and $g_3 = 3_{001}^-$ is the clockwise threefold rotation around the c axis. $g_4 = m_{1\bar{1}0}$ is a reflection perpendicular to vector $\mathbf{a} - \mathbf{b}$. $g_5 = m_{120}$ is reflection perpendicular to vector $\mathbf{a} + 2\mathbf{b}$. $g_6 = m_{210}$ is a reflection perpendicular to the vector $2\mathbf{a} + \mathbf{b}$.

According to the invariant method, $\hat{H}(\kappa) = \hat{H}^{33}$. Decomposing $\hat{\Gamma}^{\bar{\alpha}} \otimes \hat{\Gamma}^{\beta}$,

$$\bar{\Gamma}_3 \otimes \Gamma_3 = \Gamma_1 \oplus \Gamma_2 \oplus \Gamma_3.$$

Linear basis functions and the constant transform according to Γ_1 , Γ_2 , and Γ_3 of C_{3v} are listed in the following table:

γ	Γ_1	Γ_2	Γ_3
$\{H_i^{\bar{\gamma}}(\kappa)\}$	1		$\{k_+, k_-\}$

$$\hat{X}_1^1(1|\Gamma_3, \Gamma_3) \sim I = \begin{pmatrix} 1 & 0 \\ 0 & 1 \end{pmatrix},$$

$$\begin{aligned} \hat{X}_1^{\Gamma_3}(1|\Gamma_3, \Gamma_3) &\sim \begin{pmatrix} \left(\begin{array}{c|c} \bar{\Gamma}_3 \Gamma_3 & \Gamma_3 \\ 1 & 1 \end{array} \right) & \left(\begin{array}{c|c} \bar{\Gamma}_3 \Gamma_3 & \Gamma_3 \\ 1 & 1 \end{array} \right) \\ \left(\begin{array}{c|c} \bar{\Gamma}_3 \Gamma_3 & \Gamma_3 \\ 1 & 2 \end{array} \right) & \left(\begin{array}{c|c} \bar{\Gamma}_3 \Gamma_3 & \Gamma_3 \\ 1 & 2 \end{array} \right) \end{pmatrix} \\ &= \begin{pmatrix} 0 & 1 \\ 0 & 0 \end{pmatrix}, \end{aligned}$$

$$\begin{aligned} \hat{X}_2^{\Gamma_3}(1|\Gamma_3, \Gamma_3) &\sim \begin{pmatrix} \left(\begin{array}{c|c} \bar{\Gamma}_3 \Gamma_3 & \Gamma_3 \\ 2 & 1 \end{array} \right) & \left(\begin{array}{c|c} \bar{\Gamma}_3 \Gamma_3 & \Gamma_3 \\ 2 & 1 \end{array} \right) \\ \left(\begin{array}{c|c} \bar{\Gamma}_3 \Gamma_3 & \Gamma_3 \\ 2 & 2 \end{array} \right) & \left(\begin{array}{c|c} \bar{\Gamma}_3 \Gamma_3 & \Gamma_3 \\ 2 & 2 \end{array} \right) \end{pmatrix} \\ &= \begin{pmatrix} 0 & 0 \\ 1 & 0 \end{pmatrix}, \end{aligned}$$

$$\begin{aligned} \hat{H}^{33}(\kappa) &= \hat{X}_1^{\Gamma_1}(1|\Gamma_3, \Gamma_3) + 0 + \hat{X}_1^{\Gamma_3}(1|\Gamma_3, \Gamma_3)k_+ \\ &\quad + \hat{X}_2^{\Gamma_3}(1|\Gamma_3, \Gamma_3)k_- \\ &= \begin{pmatrix} C_0 & C_2 k_+ \\ C_2 k_- & C_0 \end{pmatrix}. \end{aligned}$$

It is clear that the band dispersion is linear near the K point when the SOC effect is not included.

Considering the SOC effect, $|\phi_1\rangle$ and $|\phi_2\rangle$ split into $|\phi_{1\uparrow}\rangle, |\phi_{1\downarrow}\rangle$ and $|\phi_{2\uparrow}\rangle, |\phi_{2\downarrow}\rangle$. The corresponding double-valued representation turns into $\Gamma_3 \otimes \Gamma_6 = \Gamma_4 \oplus \Gamma_5 \oplus \Gamma_6$, thus,

$$\hat{H}(\kappa) = \begin{pmatrix} \hat{H}^{44} & \hat{H}^{45} & \hat{H}^{46} \\ \hat{H}^{54} & \hat{H}^{55} & \hat{H}^{56} \\ \hat{H}^{64} & \hat{H}^{65} & \hat{H}^{66} \end{pmatrix}.$$

Decomposing the $\hat{\Gamma}^{\bar{\alpha}} \otimes \hat{\Gamma}^{\beta}$ for each submatrix:

	Γ_4	Γ_5	Γ_6
$\bar{\Gamma}_4 = \Gamma_5$	Γ_1	Γ_2	Γ_3
$\bar{\Gamma}_5 = \Gamma_4$	Γ_2	Γ_1	Γ_3
$\bar{\Gamma}_6 = \Gamma_6$	Γ_3	Γ_3	$\Gamma_1 \oplus \Gamma_2 \oplus \Gamma_3$

According to the invariant method,

$$\hat{H}^{44} = X_1^{\Gamma_1}(1|\Gamma_4, \Gamma_4),$$

$$\hat{H}^{55} = X_1^{\Gamma_1}(1|\Gamma_5, \Gamma_5),$$

$$\hat{H}^{45} = 0,$$

$$\hat{H}^{46} = X_1^{\Gamma_3}(1|\Gamma_4, \Gamma_6)k_+ + X_2^{\Gamma_3}(1|\Gamma_4, \Gamma_6)k_-$$

$$\hat{H}^{56} = X_1^{\Gamma_3}(1|\Gamma_5, \Gamma_6)k_+ + X_2^{\Gamma_3}(1|\Gamma_5, \Gamma_6)k_-,$$

$$\begin{aligned} \hat{H}^{66} &= X_1^{\Gamma_1}(1|\Gamma_6, \Gamma_6) + 0 + X_1^{\Gamma_3}(1|\Gamma_6, \Gamma_6)k_+ \\ &\quad + X_2^{\Gamma_3}(1|\Gamma_6, \Gamma_6)k_-. \end{aligned}$$

The remaining submatrices can be constructed by the Hermiticity of the Hamiltonian,

$$X_1^{\Gamma_3}(1|\Gamma_4, \Gamma_6) = \left[\begin{pmatrix} \Gamma_4 1 \\ 1 \end{pmatrix} \middle| \begin{pmatrix} \Gamma_3 \Gamma_6 \\ 1 \end{pmatrix} \right] = \begin{pmatrix} 0 & \frac{1}{\sqrt{2}} \end{pmatrix},$$

$$X_1^{\Gamma_3}(1|\Gamma_5, \Gamma_6) = \left[\begin{pmatrix} \Gamma_5 1 \\ 1 \end{pmatrix} \middle| \begin{pmatrix} \Gamma_3 \Gamma_6 \\ 1 \end{pmatrix} \right] = \begin{pmatrix} 0 & \frac{1}{\sqrt{2}} \end{pmatrix},$$

$$X_2^{\Gamma_3}(1|\Gamma_5, \Gamma_6) = \left[\begin{pmatrix} \Gamma_5 1 \\ 1 \end{pmatrix} \middle| \begin{pmatrix} \Gamma_3 \Gamma_6 \\ 2 \end{pmatrix} \right] = \begin{pmatrix} \frac{-i}{\sqrt{2}} & 0 \end{pmatrix},$$

$$X_1^{\Gamma_3}(1|\Gamma_6, \Gamma_6) = \left[\begin{pmatrix} \Gamma_6 1 \\ 1 \end{pmatrix} \middle| \begin{pmatrix} \Gamma_3 \Gamma_6 \\ 1 \end{pmatrix} \right] = \begin{pmatrix} 0 & 0 \\ -1 & 0 \end{pmatrix},$$

$$X_2^{\Gamma_3}(1|\Gamma_6, \Gamma_6) = \left[\begin{pmatrix} \Gamma_6 1 \\ 1 \end{pmatrix} \middle| \begin{pmatrix} \Gamma_3 \Gamma_6 \\ 2 \end{pmatrix} \right] = \begin{pmatrix} 0 & 1 \\ 0 & 0 \end{pmatrix}.$$

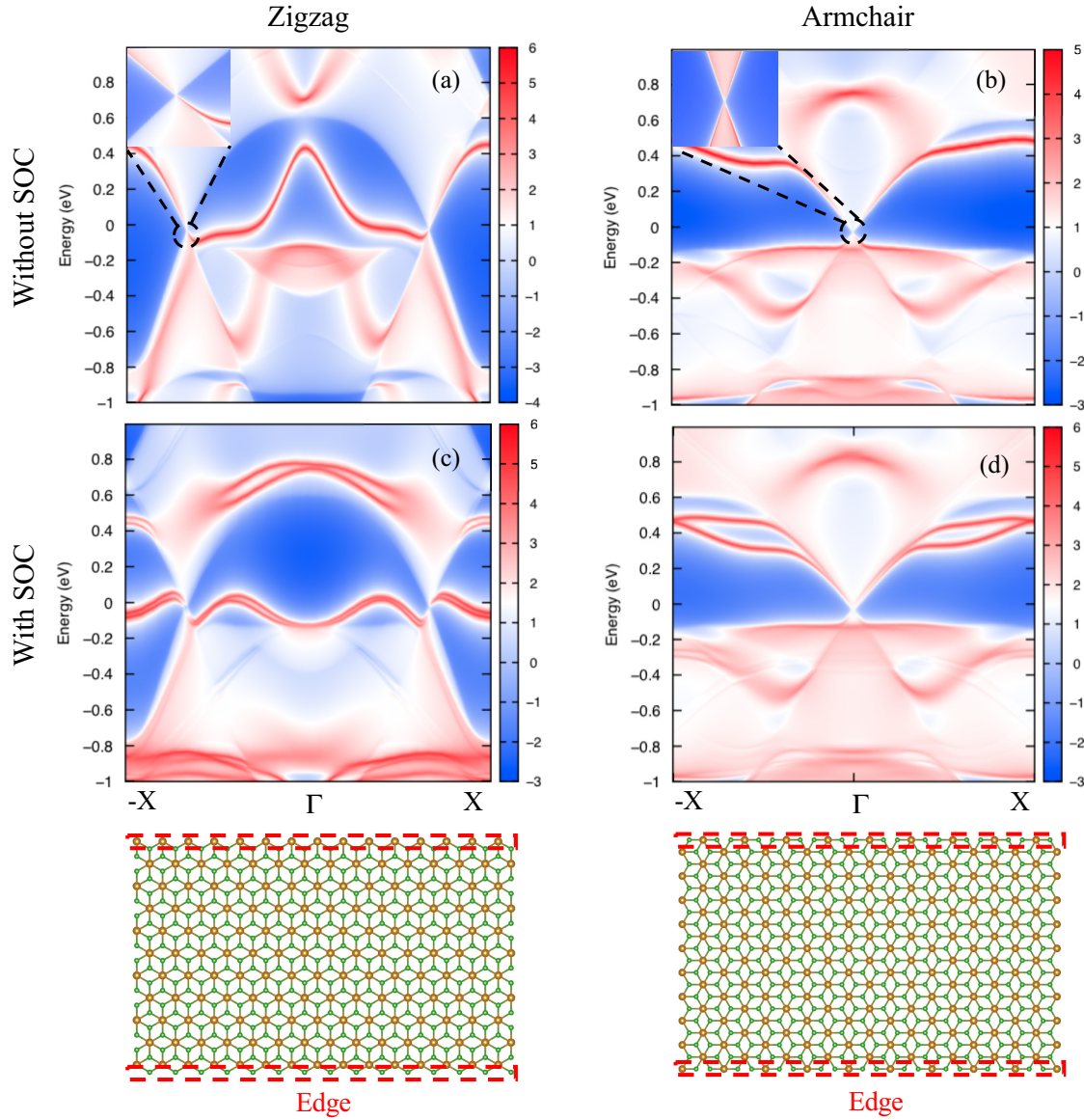


FIG. 6. Edge states of armchair and zigzag FeB₂ ribbons. The inset in (a) indicates that there exists an edge state which connects two different BCPs. This is the nontrivial edge state. For the armchair, the edge state shrinks to a point at the Γ point. The other edge states in (b) are trivial. (c) and (d) are edge states with the SOC effect taken into account.

Take these matrices together,

$$\hat{H}(\kappa) = \begin{pmatrix} a_0 & 0 & ia_1k_- & a_1k_+ \\ 0 & b_0 & -ib_1k_- & b_1k_+ \\ -ia_1k_+ & ib_1k_+ & c_0 & ic_1k_- \\ a_1k_- & b_1k_- & -ic_1k_+ & c_0 \end{pmatrix}.$$

Note that the DFT calculations show that the two bands near the Fermi level belong to the Γ_6 representation. The Dirac-like form of \hat{H}^{66} suggests that the dispersion of the two bands near the Fermi level is linear around the K point.

Note that the bases ($|\psi_1\rangle, |\psi_2\rangle, |\psi_3\rangle, |\psi_4\rangle$) of the above Hamiltonian transform according to $\Gamma_4 \oplus \Gamma_5 \oplus \Gamma_6$, which are different from the bases $|\phi_{1\uparrow}\rangle, |\phi_{1\downarrow}\rangle, |\phi_{2\uparrow}\rangle$, and $|\phi_{2\downarrow}\rangle$,

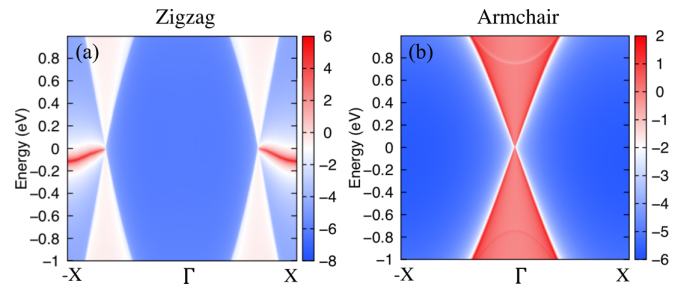


FIG. 7. Edge states of (a) zigzag and (b) armchair graphene ribbons without considering the SOC effect. For the armchair edge, the two Dirac points in the bulk system project onto the same point, thus, there is only one Dirac point for the armchair ribbon.

Now, we transform them to $|\phi_{1\uparrow}\rangle$, $|\phi_{1\downarrow}\rangle$, and $|\phi_{2\uparrow}\rangle$, $|\phi_{2\downarrow}\rangle$, that is, transforms according to $\Gamma_3 \otimes \Gamma_6$. Suppose that

$$(|\phi_{1\uparrow}\rangle, |\phi_{1\downarrow}\rangle, |\phi_{2\uparrow}\rangle, |\phi_{2\downarrow}\rangle) = (|\psi_1\rangle, |\psi_2\rangle, |\psi_3\rangle, |\psi_4\rangle)U.$$

U can be obtained by using the Clebsch-Gordan coefficient,

$$U = \begin{pmatrix} \left(\Gamma_3\Gamma_6 \middle| \Gamma_4 1\right) & \left(\Gamma_3\Gamma_6 \middle| \Gamma_5 1\right) & \left(\Gamma_3\Gamma_6 \middle| \Gamma_6 1\right) & \left(\Gamma_3\Gamma_6 \middle| \Gamma_6 1\right) \\ \left(\Gamma_3\Gamma_6 \middle| \Gamma_4 1\right) & \left(\Gamma_3\Gamma_6 \middle| \Gamma_5 1\right) & \left(\Gamma_3\Gamma_6 \middle| \Gamma_6 1\right) & \left(\Gamma_3\Gamma_6 \middle| \Gamma_6 1\right) \\ \left(\Gamma_3\Gamma_6 \middle| \Gamma_4 1\right) & \left(\Gamma_3\Gamma_6 \middle| \Gamma_5 1\right) & \left(\Gamma_3\Gamma_6 \middle| \Gamma_6 1\right) & \left(\Gamma_3\Gamma_6 \middle| \Gamma_6 1\right) \\ \left(\Gamma_3\Gamma_6 \middle| \Gamma_4 1\right) & \left(\Gamma_3\Gamma_6 \middle| \Gamma_5 1\right) & \left(\Gamma_3\Gamma_6 \middle| \Gamma_6 1\right) & \left(\Gamma_3\Gamma_6 \middle| \Gamma_6 1\right) \end{pmatrix}^\dagger = \begin{pmatrix} 0 & 1/\sqrt{2} & i/\sqrt{2} & 0 \\ 0 & 1/\sqrt{2} & -i/\sqrt{2} & 0 \\ 0 & 0 & 0 & 1 \\ -1 & 0 & 0 & 0 \end{pmatrix}$$

Hence, the Hamiltonian with bases $|\phi_{1\uparrow}\rangle$, $|\phi_{1\downarrow}\rangle$, $|\phi_{2\uparrow}\rangle$, and $|\phi_{2\downarrow}\rangle$ is

$$\hat{H}'(\kappa) = U^\dagger \hat{H}(\kappa) U$$

$$= \begin{pmatrix} c_0 & -\frac{a_1+b_1}{\sqrt{2}}k_- & -i\frac{a_1-b_1}{\sqrt{2}}k_- & ic_1k_+ \\ -\frac{a_1+b_1}{\sqrt{2}}k_+ & \frac{a_0+b_0}{2} & i\frac{a_0-b_0}{2} & i\frac{a_1-b_1}{\sqrt{2}}k_- \\ i\frac{a_1-b_1}{\sqrt{2}}k_+ & -i\frac{a_0-b_0}{2} & \frac{a_0+b_0}{2} & \frac{a_1+b_1}{\sqrt{2}}k_- \\ -ic_1k_- & -i\frac{a_1-b_1}{\sqrt{2}}k_+ & \frac{a_1+b_1}{\sqrt{2}}k_+ & c_0 \end{pmatrix}.$$

One can see that the dominant term is the first order of k_+ and k_- , thus, the dispersion is linear, in agreement with the above group-theory analysis.

APPENDIX D: EDGE STATES OF ZIGZAG AND ARMCHAIR FeB₂ NANORIBBONS

The edge states calculated without the SOC effect for the zigzag and armchair edges are shown in Fig. 6. For the

zigzag edge, the two BCPs in the bulk system are projected onto different points, which are connected by nontrivial edge states [Fig. 6(a)] that can be regarded as nearly free-electron Shockley surface states [59]. In addition, these edge states are relatively long in k space due to the long distance between the K and the K' points in the bulk system. However, for the armchair edge, since the two BCPs in the bulk system are projected onto the same point [Fig. 6(b)], the nontrivial edge states cannot be visualized here (strictly speaking, the edge states shrink to a point). We note that edge states of FeB₂ ribbons are similar to that (Fig. 7) of graphene ribbons [60]. After considering the SOC effect, the edge states of FeB₂ split, possibly due to the Rashba effect [Figs. 6(c) and 6(d)]. We also calculate the Berry phase by using a closed loop encircling a band crossing point in the 2D FeB₂ system and find that the result is π , indicating that the band crossing point is topologically nontrivial.

-
- [1] X. Wan, A. M. Turner, A. Vishwanath, and S. Y. Savrasov, *Phys. Rev. B* **83**, 205101 (2011).
- [2] A. A. Burkov and L. Balents, *Phys. Rev. Lett.* **107**, 127205 (2011).
- [3] S. L. Adler, *Phys. Rev.* **177**, 2426 (1969).
- [4] A. Burkov, *J. Phys.: Condens. Matter* **27**, 113201 (2015).
- [5] X. Huang, L. Zhao, Y. Long, P. Wang, D. Chen, Z. Yang, H. Liang, M. Xue, H. Weng, Z. Fang, X. Dai, and G. Chen *Phys. Rev. X* **5**, 031023 (2015).
- [6] G. Xu, H. Weng, Z. Wang, X. Dai, and Z. Fang, *Phys. Rev. Lett.* **107**, 186806 (2011).
- [7] A. A. Burkov, *Phys. Rev. Lett.* **113**, 187202 (2014).
- [8] E. Liu, Y. Sun, N. Kumar, L. Muechler, A. Sun, L. Jiao, S.-Y. Yang, D. Liu, A. Liang, and Q. Xu, *Nat. Phys.* **14**, 1125 (2018).
- [9] C. Shekhar, N. Kumar, V. Grinenko, S. Singh, R. Sarkar, H. Luetkens, S.-C. Wu, Y. Zhang, A. C. Komarek, and E. Kampert, *Proc. Natl. Acad. Sci. USA* **115**, 9140 (2018).
- [10] M. Yao, H. Lee, N. Xu, Y. Wang, J. Ma, O. Yazyev, Y. Xiong, M. Shi, G. Aeppli, and Y. Soh, *arXiv:1810.01514*.
- [11] Y. Sun, Y. Zhang, C. Felser, and B. Yan, *Phys. Rev. Lett.* **117**, 146403 (2016).
- [12] L. Balents, *Physics* **4**, 36 (2011).
- [13] H. B. Nielsen and M. Ninomiya, *Nucl. Phys. B* **185**, 20 (1981).
- [14] R. Yu, H. Weng, Z. Fang, H. Ding, and X. Dai, *Phys. Rev. B* **93**, 205133 (2016).
- [15] Q. Ma, S.-Y. Xu, C.-K. Chan, C.-L. Zhang, G. Chang, Y. Lin, W. Xie, T. Palacios, H. Lin, and S. Jia, *Nat. Phys.* **13**, 842 (2017).
- [16] H. B. Nielsen and M. Ninomiya, *Phys. Lett. B* **130**, 389 (1983).
- [17] H. Weng, C. Fang, Z. Fang, B. A. Bernevig, and X. Dai, *Phys. Rev. X* **5**, 011029 (2015).
- [18] J. Ruan, S.-K. Jian, H. Yao, H. Zhang, S.-C. Zhang, and D. Xing, *Nat. Commun.* **7**, 11136 (2016).
- [19] A. A. Soluyanov, D. Gresch, Z. Wang, Q. Wu, M. Troyer, X. Dai, and B. A. Bernevig, *Nature (London)* **527**, 495 (2015).
- [20] L. Yang, Z. Liu, Y. Sun, H. Peng, H. Yang, T. Zhang, B. Zhou, Y. Zhang, Y. Guo, and M. Rahn, *Nat. Phys.* **11**, 728 (2015).
- [21] Z. Wang, D. Gresch, A. A. Soluyanov, W. Xie, S. Kushwaha, X. Dai, M. Troyer, R. J. Cava, and B. A. Bernevig, *Phys. Rev. Lett.* **117**, 056805 (2016).

- [22] K. Deng, G. Wan, P. Deng, K. Zhang, S. Ding, E. Wang, M. Yan, H. Huang, H. Zhang, and Z. Xu, *Nat. Phys.* **12**, 1105 (2016).
- [23] J. Ruan, S.-K. Jian, D. Zhang, H. Yao, H. Zhang, S.-C. Zhang, and D. Xing, *Phys. Rev. Lett.* **116**, 226801 (2016).
- [24] Y. Sun, S.-C. Wu, M. N. Ali, C. Felser, and B. Yan, *Phys. Rev. B* **92**, 161107(R) (2015).
- [25] S. Nie, H. Weng, and F. B. Prinz, *Phys. Rev. B* **99**, 035125 (2019).
- [26] J. Ahn and B.-J. Yang, *Phys. Rev. Lett.* **118**, 156401 (2017).
- [27] J. Kim, S. S. Baik, S. W. Jung, Y. Sohn, S. H. Ryu, H. J. Choi, B.-J. Yang, and K. S. Kim, *Phys. Rev. Lett.* **119**, 226801 (2017).
- [28] S. M. Young and C. L. Kane, *Phys. Rev. Lett.* **115**, 126803 (2015).
- [29] J.-Y. You, C. Chen, Z. Zhang, X.-L. Sheng, S. A. Yang, and G. Su, *Phys. Rev. B* **100**, 064408 (2019).
- [30] Y. Zhang, Y. Sun, and B. Yan, *Phys. Rev. B* **97**, 041101(R) (2018).
- [31] S. Park and B.-J. Yang, *Phys. Rev. B* **96**, 125127 (2017).
- [32] S. S. Baik, K. S. Kim, Y. Yi, and H. J. Choi, *Nano Lett.* **15**, 7788 (2015).
- [33] L. Z. Zhang, Z. F. Wang, S. X. Du, H.-J. Gao, and F. Liu, *Phys. Rev. B* **90**, 161402(R) (2014).
- [34] B. J. Wieder and C. L. Kane, *Phys. Rev. B* **94**, 155108 (2016).
- [35] G. Chang, B. J. Wieder, F. Schindler, D. S. Sanchez, I. Belopolski, S.-M. Huang, B. Singh, D. Wu, T.-R. Chang, and T. Neupert, *Nature Mater.* **17**, 978 (2018).
- [36] N. P. Armitage, E. J. Mele, and A. Vishwanath, *Rev. Mod. Phys.* **90**, 015001 (2018).
- [37] H. Zhang, Y. Li, J. Hou, A. Du, and Z. Chen, *Nano Lett.* **16**, 6124 (2016).
- [38] V. M. Pereira, A. H. Castro Neto, and N. M. R. Peres, *Phys. Rev. B* **80**, 045401 (2009).
- [39] G. Montambaux, F. Piéchon, J.-N. Fuchs, and M. O. Goerbig, *Phys. Rev. B* **80**, 153412 (2009).
- [40] H. Watanabe, H. C. Po, M. P. Zaletel, and A. Vishwanath, *Phys. Rev. Lett.* **117**, 096404 (2016).
- [41] M. I. Aroyo, J. M. Perez-Mato, C. Capillas, E. Kroumova, S. Ivantchev, G. Madariaga, A. Kirov, and H. Wondratschek, *Z. Kristallogr.-Cryst. Mater.* **221**, 15 (2006).
- [42] M. Hamermesh, *Group Theory and Its Application to Physical Problems* (Courier, New York, 2012).
- [43] C.-X. Liu, X.-L. Qi, H.J. Zhang, X. Dai, Z. Fang, and S.-C. Zhang, *Phys. Rev. B* **82**, 045122 (2010).
- [44] I. Souza, N. Marzari, and D. Vanderbilt, *Phys. Rev. B* **65**, 035109 (2001).
- [45] A. A. Mostofi, J. R. Yates, Y.-S. Lee, I. Souza, D. Vanderbilt, and N. Marzari, *Comput. Phys. Commun.* **178**, 685 (2008).
- [46] Q. Wu, S. Zhang, H.-F. Song, M. Troyer, and A. A. Soluyanov, *Comput. Phys. Commun.* **224**, 405 (2018).
- [47] C. Fang and L. Fu, *Sci. Adv.* **5**, eaat2374 (2019).
- [48] K. Asano and C. Hotta, *Phys. Rev. B* **83**, 245125 (2011).
- [49] J. L. Mañes, F. Guinea, and M. A. H. Vozmediano, *Phys. Rev. B* **75**, 155424 (2007).
- [50] J. Wang, S. Deng, Z. Liu, and Z. Liu, *Natl. Sci. Rev.* **2**, 22 (2015).
- [51] K. Liu, W. Luo, J. Y. Ji, P. Barone, S. Picozzi, and H. J. Xiang, *Nat. Commun.* **10**, 5144 (2019).
- [52] W. Luo, K. Xu, and H. Xiang, *Phys. Rev. B* **96**, 235415 (2017).
- [53] Z. Fei, W. Zhao, T. A. Palomaki, B. Sun, M. K. Miller, Z. Zhao, J. Yan, X. Xu, and D. H. Cobden, *Nature (London)* **560**, 336 (2018).
- [54] C. Bradley and A. Cracknell, *The Mathematical Theory of Symmetry in Solids: Representation Theory for Point Groups and Space Groups* (Oxford University Press, Oxford, 2009).
- [55] P. E. Blöchl, *Phys. Rev. B* **50**, 17953 (1994).
- [56] G. Kresse and J. Hafner, *Phys. Rev. B* **49**, 14251 (1994).
- [57] J. P. Perdew, K. Burke, and M. Ernzerhof, *Phys. Rev. Lett.* **77**, 3865 (1996).
- [58] G. L. Bir and G. E. Pikus, *Symmetry and Strain Induced Shifts in Semiconductors* (Wiley, New York, 1974).
- [59] P. Zhang, J.-Z. Ma, Y. Ishida, L.-X. Zhao, Q.-N. Xu, B.-Q. Lv, K. Yaji, G.-F. Chen, H.-M. Weng, X. Dai, Z. Fang, X.-Q. Chen, L. Fu, T. Qian, H. Ding, and S. Shin, *Phys. Rev. Lett.* **118**, 046802 (2017).
- [60] M. Fujita, K. Wakabayashi, K. Nakada, and K. Kusakabe, *J. Phys. Soc. Jpn.* **65**, 1920 (1996).